nature geoscience

Article

https://doi.org/10.1038/s41561-023-01146-x

The magmatic architecture and evolution of the Chang'e-5 lunar basalts

Received: 13 March 2022

Accepted: 16 February 2023

Published online: 20 March 2023

Check for updates

Biji Luo[1] ✉, Zaicong Wang[1] ✉, Jiale Song[1], Yuqi Qian[1], Qi He[1], Yiheng Li[1], James W. Head[2], Frédéric Moynier[3], Long Xiao[1], Harry Becker[4], Bixuan Huang[1], Bing Ruan[1], Yangxuan Hu[1], Fabing Pan[1], Chang Xu[1], Wenlong Liu[1], Keqing Zong[1], Jiawei Zhao[1], Wen Zhang[1], Zhaochu Hu[1], Zhenbing She[1], Xiang Wu[1] & Hongfei Zhang[1]

The lunar basalt samples returned by the Chang'e-5 mission erupted about 2.0 billion years ago during the late period of the Moon's secular cooling. The conditions of mantle melting in the source region and the migration of magma through the thick lithosphere that led to this relatively late lunar volcanism remain open questions. Here we combine quantitative textural analyses of Chang'e-5 basaltic clasts, diffusion chronometry, clinopyroxene geothermobarometers and crystallization simulations to establish a holistic picture of the dynamic magmatic–thermal evolution of these young lunar basalts. We find that the Chang'e-5 basalts originated from an olivine-bearing pyroxenite mantle source (10–13 kbar or 250 ± 50 km; 1,350 ± 50 °C), similar to Apollo 12 low-Ti basalts. We propose these magmas then ascended through the plumbing system and accumulated mainly at the top of the lithospheric mantle (~2–5 kbar or 40–100 km, 1,150 ± 50 °C), where they stalled at least several hundred days and evolved via high-degree fractional crystallization. Finally, the remaining evolved melts erupted rapidly onto the surface over several days. Our magmatic–thermal evolution model indicates abundant low-solidus pyroxenites in the mantle source with a slightly enhanced inventory of radioactive elements can explain the prolonged, but declining, lunar volcanism up to about 2 billion years ago and beyond.

Volcanism is the primary endogenic process of the terrestrial planets, reflecting their internal thermal state and evolution[1,2]. Volcanic activity on the Moon is the key record of its thermo-chemical evolution[3]. Lunar mare basalts were erupted mainly in two major pulses of ~3.9–3.6 billion years ago (Ga) and ~3.4–3.1 Ga, significantly fewer were emplaced between ~3.1 and 2.0 Ga as the lunar mantle cooled, and the process finally ceased at ~1.2 Ga[4–6]. Available data suggested that the majority of the lunar mare basalts were erupted in the Procellarum KREEP Terrane (PKT), a region rich in potassium, rare-earth elements and phosphorus (KREEP)[5,7]. These observations have led to the hypothesis that the elevated KREEP in mare basalt mantle sources was the heat source for prolonging lunar volcanism[8,9] and, presumably, asymmetric thermal evolution of the Moon[10].

China's Chang'e-5 (CE-5) mission landed in northern Oceanus Procellarum within the PKT and sampled the youngest (~2.0 Ga) lunar basalts radiometrically dated so far[11,12]. However, the mantle source

[1]State Key Laboratory of Geological Processes and Mineral Resources, School of Earth Sciences, China University of Geosciences, Wuhan, China. [2]Department of Earth, Environmental and Planetary Sciences, Brown University, Providence, RI, USA. [3]Institut de Physique du Globe de Paris, Université Paris Cité, CNRS, UMR 7154, Paris, France. [4]Institut für Geologische Wissenschaften, Freie Universität Berlin, Berlin, Germany. ✉e-mail: luobj@cug.edu.cn; zaicongwang@cug.edu.cn

of the CE-5 basalts had neither a high concentration of KREEP nor abundant water[13,14], inconsistent with the hypothesis that high KREEP or volatiles in the source promoted melting. Therefore, a fundamental outstanding question is the identification of the mechanisms that led to melting of the lunar mantle at such a late evolutionary stage. Furthermore, the history of ascent, eruption and chemical evolution of lunar basalts[15,16], and the specific circumstances for the CE-5 basalts in the PKT, are of great importance for understanding late-stage lunar evolution but are poorly understood.

Geochronology, geochemistry and geological data from the landing site suggest that the returned CE-5 soil samples are dominated by local basaltic materials (>95%) and represent a single volcanic-eruption event[11–13,17,18]. On average, basaltic fragments belong to intermediate-Ti compositions (5–6 wt% TiO_2), consist of clinopyroxene (40–44%), plagioclase (29–32%), olivine (5–7%) and ilmenite (4–5%) and display diverse textures, including porphyritic, ophitic/subophitic, poikilitic and equigranular with various sizes (0.01–2.00 mm) (refs. [12,13,19,20]). Clinopyroxene and olivine show compositional zonation with more Fe-rich rims, especially clinopyroxene displaying extreme chemical zonation (for example, Mg# (100 × molar Mg/(Mg + Fe)) = 62 to 1)[13,19,20]. Preliminary mineralogical and geochemical studies show that the CE-5 basalts are products of high-degree fractional crystallization of low-Ti basaltic magmas within a large subsurface magma reservoir[13,19,21,22]. Clinopyroxenes with various types of chemical zoning can provide crucial information about the origin and storage conditions, crystallization history, timescale and dynamic processes of magma reservoirs[23–26]. Thus, the diversity of textural and mineral zoning in the CE-5 basaltic fragments provides a unique opportunity to decipher the magmatic–thermal evolution of young lunar volcanism.

One of the latest advances in terrestrial volcanology and petrology is the combination of quantitative textural analysis, geothermobarometers, diffusion chronology and thermodynamic simulations to reconstruct the entire magmatic evolution history[25,27–29]. Using such multiple approaches, we elaborate the detailed composition–pressure–temperature–time path for the origin, ascent, storage and eruption of the young CE-5 basalts. This analysis also provides key insights into the nature of lunar upper mantle and into the thermo-chemical evolution of the lunar interior when compared with lunar basalts that formed earlier.

Composition–pressure–temperature–time path for CE-5 basalts

The diverse textures of the CE-5 basalts reflect their complex crystallization history[13]. Crystal size distribution (CSD) is a quantitative textural analytical method to obtain information about the rate of crystal nucleation, residence time and magmatic processes[30] (Methods). Due to the low fraction of olivine, CSD analysis was applied to the major mineral phases of plagioclase, clinopyroxene and ilmenite in 15 CE-5 basaltic fragments (Extended Data Fig. 1 and Extended Data Table 1). Overall, the CSD patterns of all the samples collectively define a curved trend: their *y* intercepts and slopes decrease gradually with increasing crystal sizes (Fig. 1a,b). Minerals with variable intercepts and slopes reflect their different initial nucleation density (n_0) and residence time (t). Although different minerals have different shapes and sizes, three distinct populations were classified according to the crystal size, *y* intercepts and slope. Population 1 plagioclases with the smallest sizes (<0.1 mm) show the highest *y* intercepts (17.00–18.95 mm^{-4}) and steepest slopes; Population 2 minerals have intermediate sizes (0.1–0.5 mm), *y* intercepts and slope values; Population 3 minerals exhibit larger maximum crystal sizes (>0.5 mm) and lower *y* intercepts (6.58–8.07 mm^{-4}) and slope values.

Microlites in anhydrous basaltic lava flow usually reflect magma cooling rate and undercooling (ΔT) conditions in the lava channel, whereas large phenocrysts may be antecrysts from a deep magma reservoir[31]. In the chilled shallow channel, rapid quench and cooling could cause high ΔT, which drives nucleation of abundant microlites with very small sizes and high *y* intercepts[32]. In the deeper channel, crystals would continue to grow due to slowly cooling, resulting in a slight increase in size and a decrease in nucleation density[32,33]. In deep magma reservoirs, where the temperature was higher and ΔT lower, the nucleation rate was reduced, and large crystals with lower *y* intercepts tended to form[32,34]. Thus, we interpret the Population 1 and Population 2 microlites as the products of crystallization in shallow and somewhat deeper channels, respectively, whereas the larger Population 3 minerals formed in the deeper magma reservoirs. Combined with data of growth rates for plagioclase, clinopyroxene and ilmenite in basalts[35], CSD slopes were used to estimate the cooling or residence timescale of minerals (Methods). The results show that Population 1 formed by rapid cooling within ~3–8 days; Population 2 had residence times of ~10–50 days; and Population 3 showed longer residence times of ~77–105 days (Fig. 1c and Extended Data Table 1).

Clinopyroxenes, ubiquitous in all the CE-5 basaltic clasts, display a large compositional range ($En_{1-61}Fs_{23-86}Wo_{12-44}$) (Extended Data Figs. 2a and 3a,b) and can be divided into three types according to textures and chemical zonation (Fig. 2). Most clinopyroxenes (Type I), occur as either matrix microlites (I-a) or large phenocrysts (I-b) with simple core–rim texture, consistently displaying low-Mg# (5–20) thin (1–20 μm) rims, while their cores have Mg# of 30–40 or 50–60 (Fig. 2). Type II clinopyroxenes display patchy zoning, and their Mg# varies from 55–62 in the cores to 30–40 in the rims. Type III clinopyroxenes, typically with larger sizes (usually >1 mm), exhibit complex core–mantle–rim texture, including stepped normal (III-a) and reverse (III-b) zonation. The cores of Type III-a show high Mg# (50–60), the mantles have intermediate Mg# (32–42), and the thin rims display uniform low Mg# values (10–28) (Fig. 2 and Extended Data Fig. 2), implying a multistage crystallization history. Type III-b shows low-Mg# (30) cores but high-Mg# (55–60) mantles (Fig. 2), reflecting a new high-Mg# magma pulse recharging the earlier batch of evolved magmas.

Diffusion chronometry based on Mg–Fe zonation in clinopyroxene also can be used to estimate the pre-eruption residence timescale of crystals (Methods)[36]. Experiments demonstrated that the outer thin rims of minerals in volcanic rocks are commonly related to decompression- or cooling-induced growth[37]. Similarly, the outer thin rims of most clinopyroxenes are growth zonation rather than diffusion zonation. Thus, the internal zonation of Types II and III clinopyroxenes were used for Mg–Fe diffusion modelling. The results indicate that these crystals experienced at least several hundred days of residence times (Extended Data Table 2), which is comparable to the timescale obtained by the CSD method (Fig. 1c,d).

Clinopyroxenes occur across a wide range of pressures and temperatures (*P*–*T*) in basaltic magmas and thus can effectively record the crystallization history[23,24]. Most clinopyroxene microlites and phenocryst rims from CE-5 samples have low Al and Na contents and high Ti/Al atomic ratios of 1/2, indicating final co-crystallization of clinopyroxene and plagioclase[24]. However, a few grains display high Al and Na contents with low Ti/Al ratios approaching 1/4 or 1/8 (Fig. 3a–c). This observation might indicate either a single-stage[24,38] or a two-stage crystallization history[23,24,39], which can be distinguished further by the morphology and compositional characteristics of pyroxenes[23,24]. The single-stage model suggests in situ crystallization near the surface with delayed nucleation of plagioclase due to the kinetics processes induced by rapid cooling. In this situation, clinopyroxenes may occur long prismatic, skeletal, dendritic or microcrystalline, and sector zoning and thin quenched rims can be developed on pre-existing phenocrysts. Some skeletal clinopyroxenes from the Apollo 15 vitrophyric pigeonite basalt 15499[24] and long-prismatic clinopyroxenes with sector zoning from the Apollo 12 ilmenite basalt 12063/65[38] may be the crystallization products of very fast cooling of basalts, which would suppress plagioclase saturation[40] and result in the enrichment of Al and Na in clinopyroxenes (Fig. 3d). Some clinopyroxenes (041GP-001)[13]

https://doi.org/10.1038/s41561-023-01146-x

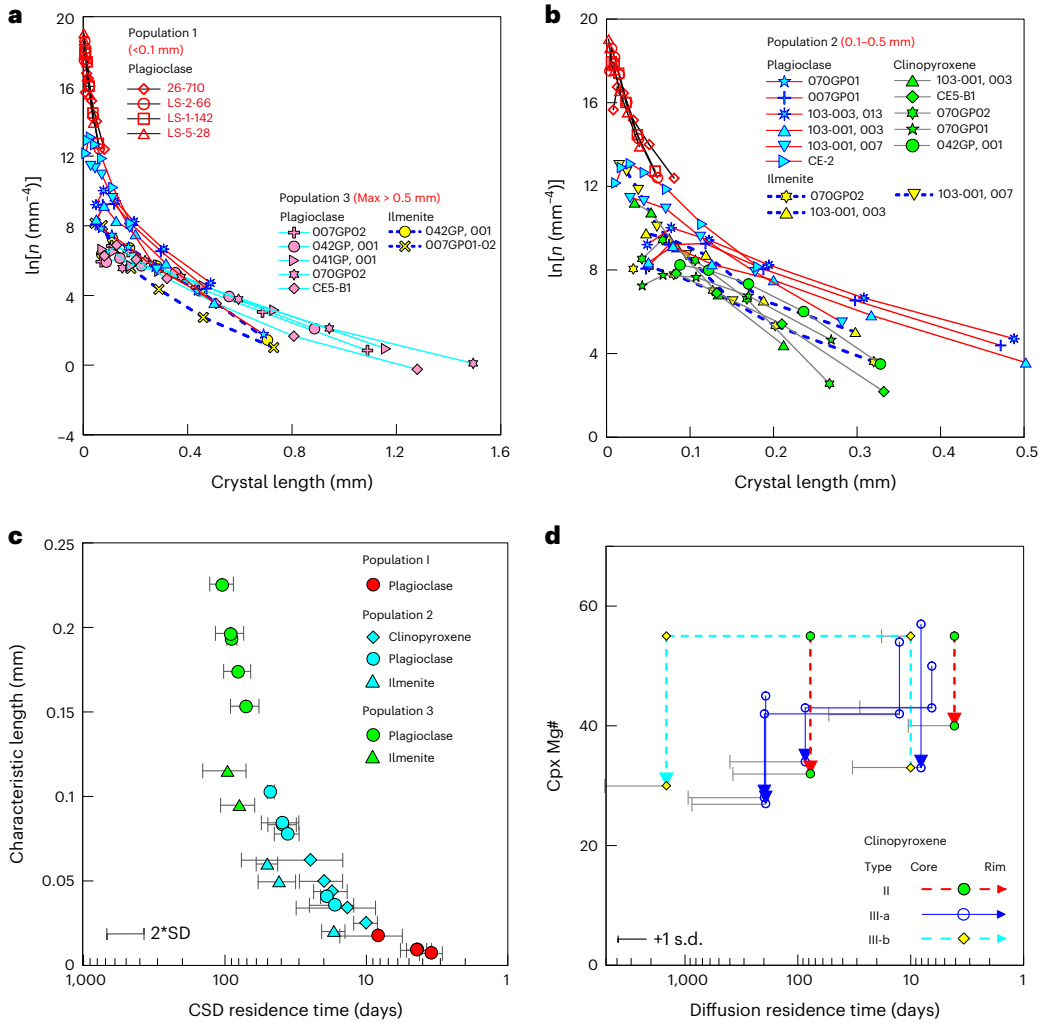

Fig. 1 | The CSD and diffusion results for the CE-5 basalts. a, The CSD patterns for plagioclase, ilmenite and clinopyroxene from the CE-5 basaltic clasts. Three distinct populations were classified according to the crystal size, nucleation density (n_0) and slope. **b**, CSD patterns for small-size Population 1 and Population 2 crystals. **c**, Residence time (days) versus characteristic length (mm). Residence times were calculated by the slopes of CSD. **d**, Diffusion times estimated from Mg–Fe exchange versus Mg# (100 × molar Mg/(Mg + Fe)) in clinopyroxene (Cpx). The arrows represent deceasing Mg# from core to rim. See Extended Data Table 1 for details of the samples plotted in **a** and **b**.

with very low Mg# (3–6) but high Al and Na contents and Ti/Al ratios (~1/8) (Fig. 3a–c) in their thin quenched rims could have formed by this mechanism.

However, a surface model is not suitable to explain the composition of other clinopyroxenes from the CE-5 samples. High Al and Na contents coupled with low Ti/Al ratios are observed mainly in larger clinopyroxene phenocryst cores with high Mg# (50–60) (Fig. 3c) rather than in long-prismatic or skeletal pyroxenes. With the decreasing Mg#, their Al decreased rapidly, and Ti/Al ratios increased rapidly from 1/4 or 1/8 to 1/2 (Fig. 3c), indicating that plagioclase had already been saturated in the early evolution stage. Some Type II and Type III clinopyroxene cores have resorption textures (Extended Data Fig. 2), implying that the melt composition and physicochemical environment of crystal growth had changed. The diffusion results (Fig. 1d) also indicate that some larger clinopyroxenes had experienced a longer residence in magma reservoirs. Experimental studies indicated that the Al contents of clinopyroxene in basaltic magmas increase with increasing pressure[41]. Therefore, we propose a two-stage model in which the large clinopyroxene phenocrysts initially began crystallizing in a magma reservoir within the lunar interior, followed by precipitation with plagioclase during the shallow eruption stage.

To quantitatively constrain the magma storage conditions recorded by the 'early' clinopyroxenes with high Mg# (50–62), the clinopyroxene–liquid thermobarometers[26,29] were used to estimate the *P*–*T* results for the CE-5 basalts (Methods). For this purpose, high-quality concentration data on clinopyroxenes in equilibrium with the host basaltic melts are required (Methods). Only 78 out of 728 analysed spots[12–14,19] provide reliable results (Supplementary Table 2), which indicate that most high-Mg# clinopyroxenes crystallized at 2–5 kbar and 1,140–1,200 °C, while some rare grains are likely to have been entrained from deeper levels (7–12 kbar and 1,260–1,300 °C) (Fig. 4a).

To further constrain the storage conditions of the CE-5 basalts, pMELTS crystallization simulations were carried out over a range of pressures (0–15 kbar) and temperatures (900–1,400 °C) at f_{O2} = ΔIW (Methods)[28]. An average composition of CE-5 basaltic fragments (CE-5A)[13] and a relatively primitive fragment (042GP-002)[13] with higher Mg# (47) were used as starting melt composition (Extended Data Table 3). The pMELTS results also confirm that Al and Na contents in clinopyroxene increase with increasing pressure (Extended Data Fig. 6e,f). In the diagram representing the Na versus Al composition of the clinopyroxene (Fig. 3a), most crystals fall in the overlapping composition fields that crystallized at 0–3 kbar and 4–7 kbar, but several grains plot in the

https://doi.org/10.1038/s41561-023-01146-x

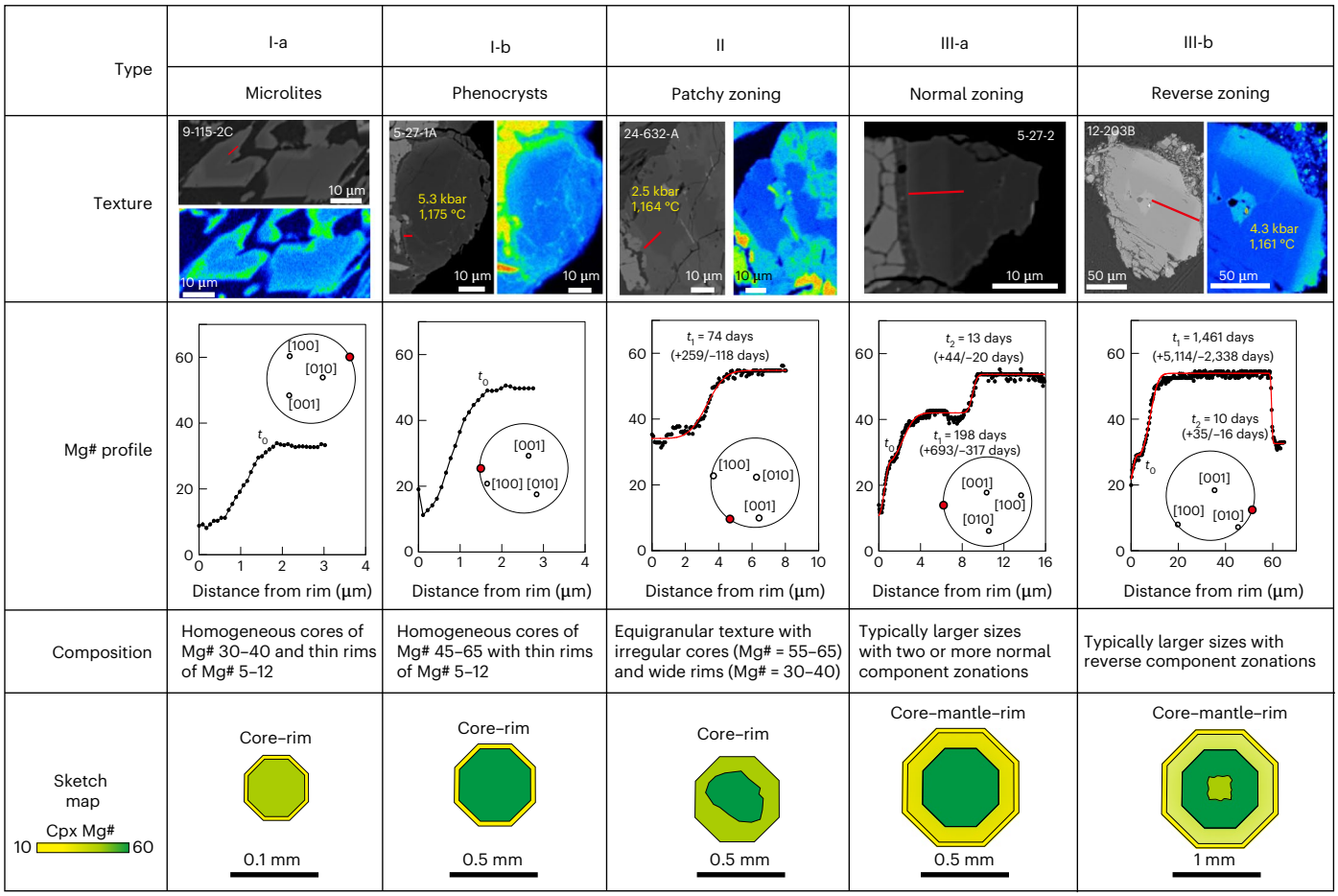

Fig. 2 | The backscattered electron (BSE) images and X-ray colour maps of Fe content and the corresponding Mg# profiles show different types of clinopyroxenes. Type I has normal core–rim textures with variable cores but thin low-Mg# (5–20) rims. I-a, microlites; I-b, phenocrysts. Type II with patchy zoning shows Mg# of 55–62 to 30–40 from cores to rims. Type III, typically larger sizes (>1 mm), exhibits core–mantle–rim textures, including normal (III-a) and reverse (III-b) zonations. Red lines on the BSE images represent the traverse profiles. The black dots of profiles represent the Mg# components calculated from the grey values of the BSE images; red lines represent diffusion model profiles. The yellow marks (for example, 5.3 kbar, 1,175 °C) on clinopyroxene images represent the estimated temperature and pressure results[26,29]. Inset circles display the projected crystallographic and traverse orientation measured by electron backscatter diffraction (EBSD).

area of 8–12 kbar, which is consistent with the results calculated using the clinopyroxene–liquid thermobarometer.

The key to an accurate determination of the CE-5 basalt's mantle source relies mainly on information on a good estimate of a representative primary magma composition. Chemical similarities suggested that the CE-5 basalts probably evolved from low-Ti basalts, similar to the Apollo 12 low-Ti basalts[13,19,22]. Experiments that studied the chemical evolution trend of the little-fractionated low-Ti basaltic sample 12002[40,42] (Mg# = 55), and the relatively primitive basaltic fragment (042GP-002)[13] and average CE-5 basaltic fragment (CE-5A)[13] and soil (CE-5S)[18,20] compositions all plot on the liquid line of descent of the Apollo 12 low-Ti basalts[40,42] (Fig. 4b), further supporting the preceding interpretation[13,19,22]. Thus, the CE-5 basalt's mantle source would be very similar to the Apollo 12 low-Ti basalts, but with a lower degree of melting for the former. The pMELTS results also indicated that most CE-5 basaltic fragments can be generated through high-degree (>30%) fractional crystallization of the magma represented by clast 042GP-002[13] (Fig. 4b).

The multiple-saturation point in the phase diagram is very helpful to constrain the residual minerals and estimate the minimum source melting depth[43]. The pMELTS simulations (Fig. 4a and Extended Data Fig. 6a–d) indicate that the CE-5 basalt's mantle source was saturated predominantly with clinopyroxene with subordinate olivine. The corresponding *P*–*T* result (10 kbar versus 1,320 °C) for the primitive CE-5 sample 042GP-002 defines the lower-limit condition for the origin of the CE-5 basalts. Recent models suggested very high pressure–temperature conditions (22–27 kbar versus 1,470–1,500 °C) for the deep source of CE-5 magma[44]; however, such conditions (similar to those for yellow and red picritic glasses[45]) would be too high to be reconciled with petrological and geochemical features of CE-5 basalts. Instead, we propose that the *P*–*T* conditions (13 kbar versus 1,380 °C) for the near-primary low-Ti basaltic sample 12002[40,42] could provide an upper bound. Thus, the CE-5 basalts could have originated from an olivine–pyroxenite source at 1,350 ± 50 °C and 10–13 kbar (250 ± 50 km) (Fig. 4a), corresponding to the upper part of the lunar mantle.

Architecture of magma plumbing system

Based on the above evidence, an integrated architecture and dynamic model of the magma plumbing system for the generation, ascent and eruption of the CE-5 basalts is proposed (Fig. 5). The pressure results (Figs. 3a and 5a) suggest that multiple magma reservoirs could have been distributed throughout the upper part of the lunar lithospheric mantle, feeding magmas into shallower levels and ultimately to the

https://doi.org/10.1038/s41561-023-01146-x

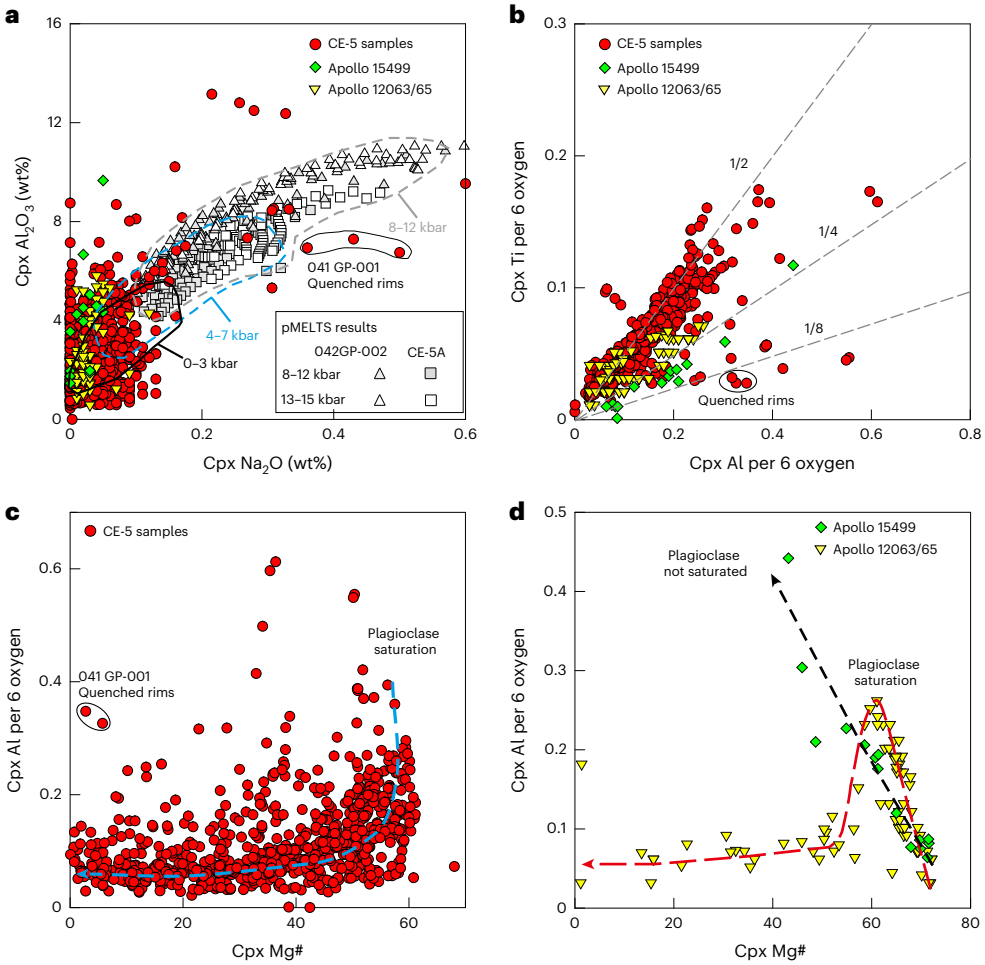

Fig. 3 | The chemical compositions of clinopyroxene (Cpx) from the CE-5 basalts and their comparison with those of some representative Apollo basaltic samples. **a**, Comparison of Na_2O and Al_2O_3 contents of Cpx from the CE-5 basalts with those of pMELTS modelling results. Cpx compositions of CE-5 samples are from this study and literature[12,13,18]. **b**, Atomic Ti versus Al crystallization trend for the CE-5 samples. Apollo samples (15499 and 12063/66) are shown for comparison. **c**, Molar Mg# versus atomic Al trend for the CE-5 samples. **d**, Molar Mg# versus atomic Al trend for the Apollo samples of 15499 and 12063/66.

surface. Overall, the CE-5 basalts experienced mainly a three-stage, polybaric magmatic evolution history.

Partial melting of clinopyroxene-rich mantle cumulates at a depth of ~250 km generated near-primary low-Ti basalts. However, the mantle source temperature of CE-5 basalts would have been lower by ~50 °C or more compared with Apollo 12 low-Ti basalts (Fig. 4a), resulting in lower degrees of melting. Partial melts from such a source were buoyant compared with the surrounding mantle (2.9–3.0 g cm^{-3} versus 3.2 g cm^{-3})[43,46] (Fig. 5b) and thus ascended due to the density contrast[15,16]. Some high-Mg# olivine and clinopyroxene with minor spinel may have crystallized during the initial ascent.

The ascending evolved melts did not erupt directly onto the surface, but instead are interpreted to have stalled at peak pressures of 2–5 kbar, corresponding to a depth of ~40–100 km (Fig. 5a,c), due to the predicted rheological and density traps between the cooled and thickened lithospheric mantle and the base of low-density crust[15,16] (Fig. 5b). Because the crustal thickness in the central PKT region has been estimated to be ~30 km (ref. [47]), the ascending melts accumulated and formed shallower magma reservoirs near the top of the lithospheric mantle, where high-degree fractional crystallization occurred. The continuous fractionation crystallization of Ti-poor minerals (for example, olivine, clinopyroxene and plagioclase) in the early stage resulted in the enrichment of Ti in the evolved melts (Fig. 4a). Ilmenite only was saturated at lower pressure (<5 kbar) as the magma approached the solidus temperature near the surface (Fig. 4a). Abundant larger plagioclase, ilmenite and clinopyroxene crystallized in the main magma reservoirs with a longer residence time of at least several hundred days (Figs. 1c,d and 5e). Type III clinopyroxenes with complex zonings imply that their host magmas had experienced a multistage polybaric crystallization and magma recharge history.

When the accumulated magma reached a sufficient overpressure to overcome the rheological and density barriers, the residual magma rapidly erupted onto the lunar surface (Fig. 5c). A large fraction of microlites also crystallized during the eruption. Population 2 crystals are likely to have crystallized in the deeper channel with a residence time of ~10–50 days, whereas Population 1 plagioclases were products of rapid quench during final fast ascent and eruption (several days) (Fig. 5f). The rapidly ascending magma entrained some antecrysts from deep regions. The various types of clinopyroxene with low-Mg# thin rims, regardless of their high-Mg# (30–40 or 50–60) cores (Fig. 2), suggest that clinopyroxenes at different evolutionary stages directly erupted to the surface and led to the ubiquitous thin rims. The rapid eruption of CE-5 magmas in northern Oceanus Procellarum produced the Em4/P58 unit and formed Rima Sharp, the most likely lava channel of CE-5 basalts, just ~15 km from the landing site[17].

https://doi.org/10.1038/s41561-023-01146-x

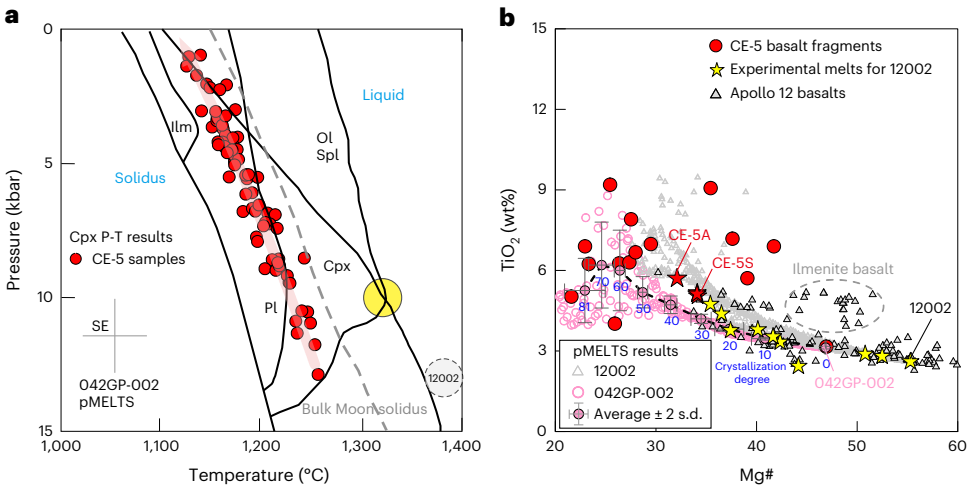

Fig. 4 | Pressure and temperature estimations and pMELTS modelling results. **a**, Pressure and temperature results of clinopyroxene–melt thermobarometry[26,29] for the CE-5 basalts and pMELTS phase diagram for 042GP-02. The shaded circles represent the multiple-saturation point indicating potential source region. The yellow shaded circle is for CE-5 basalts; the grey shaded circle is for 12002 (see details in Extended Data Fig. 6a[40]). Bulk Moon solidus[8] is also shown. **b**, Bulk-rock Mg# versus TiO_2 contents for CE-5 basalt fragments[12,13], pMELTS melts of 042GP-02 and 12002 and experimental melts for 12002[40]. The Apollo 12 low-Ti basalts are from Clive Neal's Mare Basalt database (https://www3.nd.edu/~cneal/Lunar-L/). The 042GP-02[13] basaltic fragment with a higher Mg# (47) represents a relatively primitive composition. CE-5A[13] and CE-5S[18,20] represent the average compositions of basaltic fragments and soils, respectively. Pl, plagioclase; Cpx, clinopyroxene; Ol, olivine; Ilm, ilmenite; Spl, spinel.

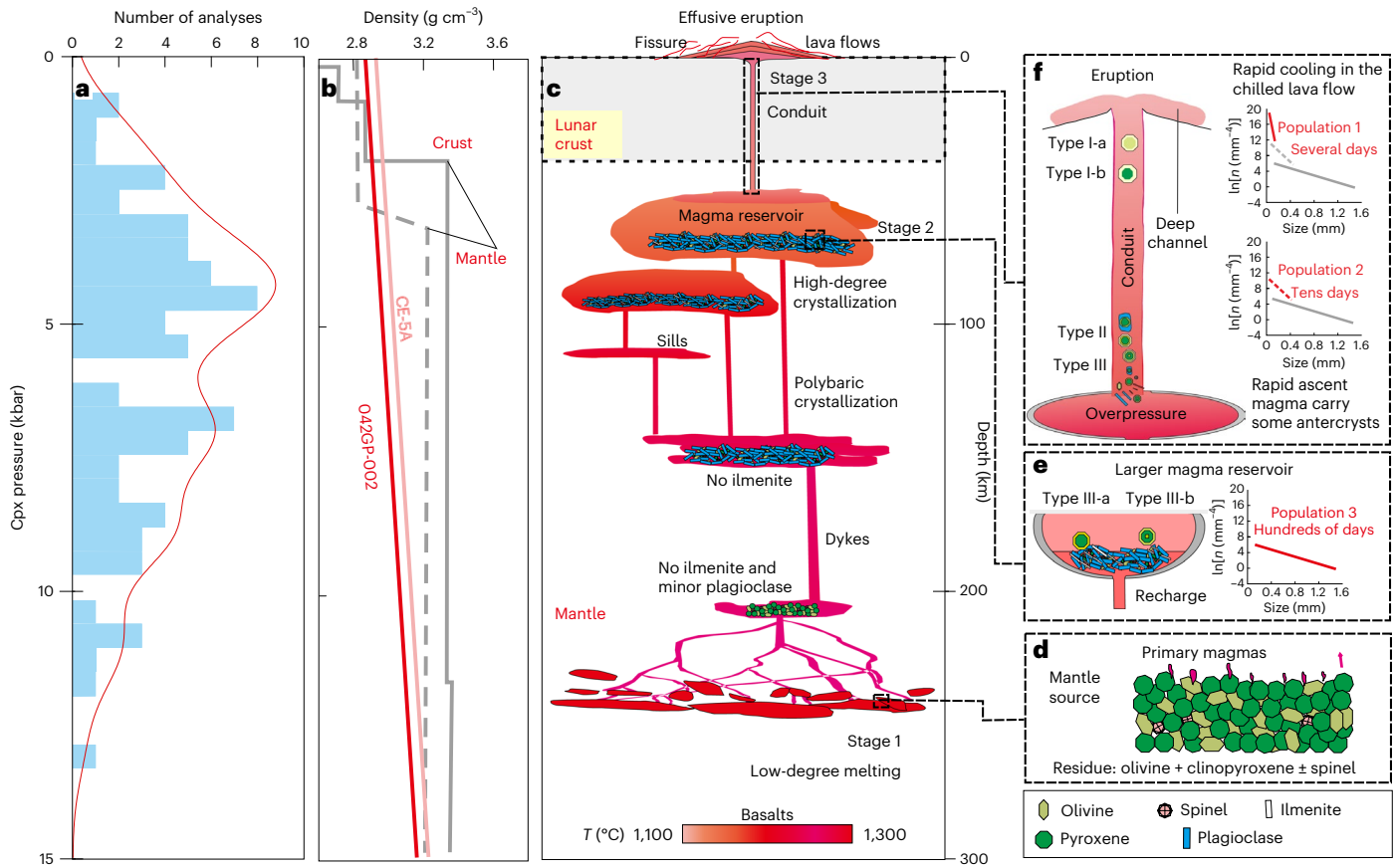

Fig. 5 | Schematic architecture model of the magma plumbing system for the young CE-5 basalts. **a**, Histogram showing the distribution of the results of clinopyroxene–melt barometry[26]. **b**, Density of CE-5A[13] and 042GP-002[13] calculated by pMELTS. Densities of lunar crust and mantle (grey dashed line[43] and grey line[46]) are also shown. **c**, The magma plumbing system of the CE-5 basalts. **d**, Low-degrees partial melting of an olivine–pyroxenite generates primary low-Ti magmas. **e**, The ascending melts stalled towards the top of lithospheric mantle due to the density and rheological traps, forming the main magma reservoirs at a depth of 2–5 kbar (40–100 km), where the magmas underwent extensive fractional crystallization. **f**, In the eruption conduit, the magma erupted rapidly onto the lunar surface. See text for details.

Clinopyroxene-rich mantle and prolonged lunar magmatism

Previous studies suggested that late lunar magmatism could be promoted by the presence of a KREEP component in the mantle source[6,9]. Sr–Nd isotopes of the CE-5 basalts were interpreted to reflect a non-KREEP mantle source[13], and KREEP was proposed to be unnecessary to promote late mantle melting[13,48]. However, a slightly higher μ value ($^{206}Pb/^{204}Pb$: 684)[11,12] and KREEP-like trace elements of the CE-5 soils and basaltic fragments[18] reveal that a small fraction (~1%) of KREEP component was involved in the mantle source[12,18]. The KREEP-like materials could be the former trapped interstitial liquid in the lunar mantle cumulate[49], and its specific fraction depends on the clinopyroxene proportion that balances KREEP to explain the Sr–Nd isotopic compositions of the CE-5 basalt's mantle source[18]. Minor KREEP-bearing material in the mantle source, long-term radioactive decay and heat accumulation may facilitate melting. Moreover, as demonstrated above, the CE-5 basalt's mantle source is composed of olivine-bearing pyroxenites[18,44], which are susceptible to melting given their low-solidus temperature[49–51].

The multiple saturation points of lunar picritic glasses and basalts have constrained the minimum *P*–*T* conditions for the formation of lunar basalts erupted at 3.9–2.9 Ga (refs. [43,45]); and the mantle potential temperature was proposed to be 1,450 ± 50 °C between 4.0 and 3.1 Ga (ref. [45]). This study suggests a mantle source region for CE-5 basalt at a depth of ~250 km with a temperature of 1,350 ± 50 °C (Fig. 4a). Thus, the source temperature for the CE-5 basalts at ~2.0 Ga was lower by around 50 °C or more relative to the ancient low-Ti basalts (3.3–3.1 Ga), indicating a slow cooling rate of the lunar interior underneath the PKT. The slow cooling of the mantle underneath this area could reflect the presence of a thicker KREEP layer at the base of the crust[8,10] or megaregolith insulation[52]. Alternatively, a minor KREEP component may have been variably dispersed in the deeper mantle, leading to on average higher heat production beneath some PKT regions. In conclusion, locally clinopyroxene-rich upper mantle with a slightly enhanced inventory of KREEP could be a reasonable environment to extend mantle melting to the late phase of lunar evolution, potentially explaining the continuation of lunar volcanism until 2.0 Ga or later.

Online content

Any methods, additional references, Nature Portfolio reporting summaries, source data, extended data, supplementary information, acknowledgements, peer review information; details of author contributions and competing interests; and statements of data and code availability are available at https://doi.org/10.1038/s41561-023-01146-x.

References

1. Wilson, L. Volcanism in the Solar System. *Nat. Geosci.* **2**, 389–397 (2009).
2. Head, J. W. & Wilson, L. Planetary volcanology: progress, problems, and opportunities. *Bull. Volcanol.* **84**, 23 (2022).
3. Shearer, C. K. et al. Thermal and magmatic evolution of the Moon. *Rev. Mineral. Geochem.* **60**, 365–518 (2006).
4. Hiesinger, H., Head, J. W., Wolf, U., Jaumann, R. & Neukum, G. Ages and stratigraphy of mare basalts in Oceanus Procellarum, Mare Nubium, Mare Cognitum, and Mare Insularum. *J. Geophys. Res. E* **108**, 5065 (2003).
5. Hiesinger, H., Head, J. W., Wolf, U., Jaumann, R. & Neukum, G. in *Recent Advances and Current Research Issues in Lunar Stratigraphy* (eds Ambrose, W. A. & Williams, D. A.) Ch. 1 (GSA, 2011).
6. Merle, R. E. et al. Pb–Pb ages and initial Pb isotopic composition of lunar meteorites: NWA 773 clan, NWA 4734, and Dhofar 287. *Meteorit. Planet. Sci.* **55**, 1808–1832 (2020).
7. Jolliff, B. L., Gillis, J. J., Haskin, L. A., Korotev, R. L. & Wieczorek, M. A. Major lunar crustal terranes: surface expressions and crust–mantle origins. *J. Geophys. Res. Planets* **105**, 4197–4216 (2000).
8. Wieczorek, M. A. & Phillips, R. J. The 'Procellarum KREEP Terrane': implications for mare volcanism and lunar evolution. *J. Geophys. Res. Planets* **105**, 20417–20430 (2000).
9. Borg, L., Shearer, C., Asmerom, Y. & Papike, J. Prolonged KREEP magmatism on the Moon indicated by the youngest dated lunar igneous rock. *Nature* **432**, 209–211 (2004).
10. Laneuville, M., Wieczorek, M. A., Breuer, D. & Tosi, N. Asymmetric thermal evolution of the Moon. *J. Geophys. Res. Planets* **118**, 1435–1452 (2013).
11. Li, Q.-L. et al. Two-billion-year-old volcanism on the Moon from Chang'e-5 basalts. *Nature* **600**, 54–58 (2021).
12. Che, X. et al. Age and composition of young basalts on the Moon, measured from samples returned by Chang'e-5. *Science* **374**, 887–890 (2021).
13. Tian, H.-C. et al. Non-KREEP origin for Chang'e-5 basalts in the Procellarum KREEP Terrane. *Nature* **600**, 59–63 (2021).
14. Hu, S. et al. A dry lunar mantle reservoir for young mare basalts of Chang'e-5. *Nature* **600**, 49–53 (2021).
15. Wilson, L. & Head, J. W. Generation, ascent and eruption of magma on the Moon: new insights into source depths, magma supply, intrusions and effusive/explosive eruptions (part 1: theory). *Icarus* **283**, 146–175 (2017).
16. Head, J. W. & Wilson, L. Generation, ascent and eruption of magma on the Moon: new insights into source depths, magma supply, intrusions and effusive/explosive eruptions (part 2: predicted emplacement processes and observations). *Icarus* **283**, 176–223 (2017).
17. Qian, Y., Xiao, L., Head, J. W. & Wilson, L. The long sinuous rille system in northern Oceanus Procellarum and its relation to the Chang'e-5 returned samples. *Geophys. Res. Lett.* **48**, e2021GL092663 (2021).
18. Zong, K. et al. Bulk compositions of the Chang'e-5 lunar soil: insights into chemical homogeneity, exotic addition, and origin of landing site basalts. *Geochim. Cosmochim. Acta* **335**, 284–296 (2022).
19. He, Q. et al. Detailed petrogenesis of the unsampled Oceanus Procellarum: the case of the Chang'e-5 mare basalts. *Icarus* **383**, 115082 (2022).
20. Li, C. et al. Characteristics of the lunar samples returned by the Chang'e-5 mission. *Natl Sci. Rev.* https://doi.org/10.1093/nsr/nwab188 (2021).
21. Yang, W. et al. Geochemistry of impact glasses in the Chang'e-5 regolith: constraints on impact melting and the petrogenesis of local basalt. *Geochim. Cosmochim. Acta* **335**, 183–196 (2022).
22. Zhang, D. et al. Titanium in olivine reveals low-Ti origin of the Chang'e-5 lunar basalts. *Lithos* **414–415**, 106639 (2022).
23. Bence, A. E., Papik, J. J. & Lindsley, D. Crystallization histories of clinopyroxenes in two porphyritic rocks from Oceanus Procellarum. In *Proc. Second Lunal Science Conference* Vol. I, 559–574 (MIT Press, 1971).
24. Bence, A. E. & Papike, J. J. Pyroxenes as recorders of lunar basalt petrogenesis: chemical trends due to crystal–liquid interaction. *Geochim. Cosmochim. Acta* **3**, 431–469 (1972).
25. Costa, F., Shea, T. & Ubide, T. Diffusion chronometry and the timescales of magmatic processes. *Nat. Rev. Earth Environ.* **1**, 201–214 (2020).
26. Neave, D. A. & Putirka, K. D. A new clinopyroxene–liquid barometer, and implications for magma storage pressures under Icelandic rift zones. *Am. Mineral.* **102**, 777–794 (2017).
27. Blundy, J. & Cashman, K. Petrologic reconstruction of magmatic system variables and processes. *Rev. Mineral. Geochem.* **69**, 179–239 (2008).
28. Ghiorso, M. S., Hirschmann, M. M., Reiners, P. W. & Kress, V. C. III The pMELTS: a revision of MELTS for improved calculation of

phase relations and major element partitioning related to partial melting of the mantle to 3 GPa. *Geochem. Geophys. Geosyst.* https://doi.org/10.1029/2001GC000217 (2002).
29. Putirka, K. D. Thermometers and barometers for volcanic systems. *Rev. Mineral. Geochem.* **69**, 61–120 (2008).
30. Marsh, B. D. Crystal size distribution (CSD) in rocks and the kinetics and dynamics of crystallization. *Contrib. Mineral. Petrol.* **99**, 277–291 (1988).
31. Cashman, K. V. Crystal Size distribution (CSD) analysis of volcanic samples: advances and challenges. *Front. Earth Sci.* **8**, 291 (2020).
32. Webb, S. et al. Crystal size distribution of plagioclase in basalt fragments from Oceanus Procellarum recovered by Chang'e-5. in *53rd Lunar and Planetary Science Conference*, 2896 (2022).
33. Brugger, C. R. & Hammer, J. E. Crystal size distribution analysis of plagioclase in experimentally decompressed hydrous rhyodacite magma. *Earth Planet. Sci. Lett.* **300**, 246–254 (2010).
34. Neal, C. R. et al. Crystal size distribution of ilmenite in Chang'e 5 basalt clasts. in *53rd Lunar and Planetary Science Conference* 2353 (2022).
35. Burkhard, D. J. M. Nucleation and growth rates of pyroxene, plagioclase, and Fe-Ti oxides in basalt under atmospheric conditions. *Eur. J. Mineral.* **17**, 675–685 (2005).
36. Müller, T., Dohmen, R., Becker, H. W., ter Heege, J. H. & Chakraborty, S. Fe–Mg interdiffusion rates in clinopyroxene: experimental data and implications for Fe–Mg exchange geothermometers. *Contrib. Mineral. Petrol.* **166**, 1563–1576 (2013).
37. Riker, J. M., Cashman, K. V., Rust, A. C. & Blundy, J. D. Experimental constraints on plagioclase crystallization during H_2O- and H_2O-CO_2-saturated magma decompression. *J. Petrol.* **56**, 1967–1998 (2015).
38. Hollister, L. S., Trzcienski, W. E.Jr., Hargraves, R. B. & Kulick, C. G. Petrogenetic significance of pyroxenes in two Apollo 12 samples. In *Proc. Second Lunar Science Conference* Vol. 2, 529–557 (MIT Press, 1971).
39. Boyd, F. & Smith, D. Compositional zoning in pyroxenes from lunar rock 12021, Oceanus Procellarum. *J. Petrol.* **12**, 439–464 (1971).
40. Walker, D., Kirkpatrick, R. J., Longhi, J. & Hays, J. F. Crystallization history of lunar picritic basalt sample 12002: phase-equilibria and cooling-rate studies. *GSA Bull.* **87**, 646–656 (1976).
41. Green, D. H., Ringwood, A. E., Ware, N. G., Hibberson, W. O. & Kiss, E. Experimental petrology and petrogenesis of Apollo 12 basalts. In *Proc. Second Lunar Science Conference* Vol. 1, 601–615 (MIT Press,1971).
42. Grove, T. L., Walker, D., Longhi, J., Stolper, E. & Hays, J. F. Petrology of rock 12002 and origin of picritic basalts at Oceanus Procellarum. In *Proc. Fourth Lunar Science Conference* (*Supplement 4*, *Geochim. Cosmochim. Acta*) Vol. 1, 995–1011 (Lunar and Planetary Institute, 1973).
43. Grove, T. L. & Krawczynski, M. J. Lunar mare volcanism: where did the magmas come from? *Elements* **5**, 29–34 (2009).
44. Su, B. et al. Fusible mantle cumulates trigger young mare volcanism on the Cooling Moon. *Sci. Adv.* **8**, eabn2103 (2022).
45. Elkins-Tanton, L. T., Hager, B. H. & Grove, T. L. Magmatic effects of the lunar late heavy bombardment. *Earth Planet. Sci. Lett.* **222**, 17–27 (2004).
46. Weber, R. C., Lin, P.-Y., Garnero, E. J., Williams, Q. & Lognonné, P. Seismic detection of the lunar core. *Science* **331**, 309–312 (2011).
47. Wieczorek, M. A. et al. The crust of the Moon as seen by GRAIL. *Science* **339**, 671–675 (2013).
48. Elardo, S. M. et al. The origin of young mare basalts inferred from lunar meteorites Northwest Africa 4734, 032, and LaPaz Icefield 02205. *Meteorit. Planet. Sci.* **49**, 261–291 (2014).
49. Snyder, G. A., Taylor, L. A. & Neal, C. R. A chemical model for generating the sources of mare basalts: Combined equilibrium and fractional crystallization of the lunar magmasphere. *Geochim. Cosmochim. Acta* **56**, 3809–3823 (1992).
50. Elkins-Tanton, L. T., Burgess, S. & Yin, Q.-Z. The lunar magma ocean: reconciling the solidification process with lunar petrology and geochronology. *Earth Planet. Sci. Lett.* **304**, 326–336 (2011).
51. Lin, Y., Tronche, E. J., Steenstra, E. S. & van Westrenen, W. Evidence for an early wet Moon from experimental crystallization of the lunar magma ocean. *Nat. Geosci.* **10**, 14–18 (2017).
52. Warren, P. H., Haack, H. & Rasmussen, K. L. Megaregolith insulation and the duration of cooling to isotopic closure within differentiated asteroids and the Moon. *J. Geophys. Res. Solid Earth* **96**, 5909–5923 (1991).

Methods

Mineral textures and compositions

Backscattered electron (BSE) images, X-ray intensity maps and chemical compositions of the mineral crystals were determined at the State Key Laboratory of Geological Processes and Mineral Resources, China University of Geosciences, Wuhan, with a JEOL JXA-8230 electron probe microanalyser equipped with five wavelength-dispersive spectrometers. The samples were first coated with a thin conductive carbon film before analysis. The carbon film thickness produced an ~10–15 nm uniform coating.

An accelerating voltage of 15 kV, a beam current of 20 nA and a 1 μm spot size were used to analyse mineral compositions. Data were corrected online using a ZAF (atomic number, absorption, fluorescence) correction procedure. The peak counting time was 10 s for Na, Mg, Al, Si, K, Ca, Fe, Cr and Ni and 20 s for Mn and Ti. The background counting time was one-half of the peak counting time on the high- and low-energy background positions. The following standards were used: jadeite (Na), olivine (Si), diopside (Ca, Mg), sanidine (K), rutile (Ti), almandine garnet (Fe, Al), rhodonite (Mn), chromium oxide (Cr) and pentlandite (Ni). The analysis accuracy is better than 1% when the content of major elements is greater than 5%, and better than 5% when the content of major elements is 1–5%. The analysed results are given in Supplementary Table 1.

X-ray intensity maps were also acquired with this electron probe microanalyser operating at 15 keV, 30 nA and a counting time of 10 ms per pixel. Kα (Si, Fe, Ca, Mg and Ti) peak intensities were collected using large TAP (thallium acid phthalate), PET (pentanerythritol) and LiF (lithium fluoride) monochromator crystals. To investigate the repartition of the five elements identified in the clinopyroxene, the analysed area was scanned as the simultaneously detected elements were constrained by the number of available spectrometers. The elemental maps were recorded by stage rastering using a stationary beam with a spatial resolution of 0.5–0.7 μm pixel^{-1}.

Crystal size distribution (CSD)

CSD is a quantitative method to obtain information about the rate of nucleation, residence time and magmatic processes[30,53]. Classical CSD is generally shown as the diagram of the natural logarithm of population density ln(n) (n is the crystal number in per unit area, mm^{-4}) versus crystal size (L, in mm). The equation for the relationship between ln(n) and L is usually expressed as:

$$\ln(n) = \ln(n^0) + \frac{-1}{G\tau} \times L \quad (1)$$

Where the intercept on the y axis at $L = 0$ is ln(n^0), and n^0 is initial nucleation density. Slope is $-1/G\tau$, where G is the growth rate and τ is the residence time.

Here the BSE images of CE-5 basalt clasts (Extended Data Fig. 1 and Extended Data Table 1) for CSD analysis were obtained from the China National Space Administration[54], published literature[11–13] and this study. Textural results show that plagioclase, clinopyroxene and ilmenite are abundant and euhedral. Thus, these minerals from a total 15 of the CE-5 basaltic clasts that were analysed. The outlines of the crystals were manually identified with the Bzier tool in CorelDraw. Moreover, some important parameters for CSD analysis, including major and minor axis lengths, roundness, circular degree, area and area proportion, were obtained from the image-processing programme ImageJ. The acquired data from two-dimensional sections were converted into three dimensions by CSDSlice[55]. Stereological corrections were undertaken using the CSDCorrections programme to calculate and obtain the logarithmic plot of the population density versus the mineral size[56].

For reliability, CSD analysis generally requires a minimum of 75 crystals for tabular minerals and 250 crystals for acicular minerals[55]. The slopes and intercepts of the CSD curves were obtained by regression analysis in Microsoft Excel. To evaluate the reliability of quantitative textural analysis, the goodness-of-fit straight line can be tested by R^2 (the degree of fit of the regression line to the observed values) obtained from linear regression[56]. Thus, some important parameters, such as residence time ($\tau = -1/G \times$ slope) and characteristic length ($C_L = -1$/slope), can be calculated. The fitting error of slope is also used to calculate the error of residence time.

The growth rate G of minerals is obtained from experimental study and natural observation on modern active volcanoes. This parameter is crucial to accurately estimate the residence time but usually shows a certain range of variation. For example, plagioclase growth rate can vary from 10^{-6} to 10^{-10} mm s^{-1} (over 5 log units)[33]. Previous studies have shown that the cooling rate plays a decisive role in the G of plagioclase, regardless of its host magma composition[33]. In the case of slow cooling, G for plagioclase varies from 10^{-8} to 10^{-10} mm s^{-1}, while in the case of fast cooling, plagioclase G can reach 10^{-6} to 10^{-8} mm s^{-1}. The residence time of plagioclase calculated by G of 10^{-8} mm s^{-1} is consistent with the duration of the experimental results[33]. Thus, experimentally determined growth rates (2.49×10^{-8} mm s^{-1}) of basaltic plagioclase were applied to this study[35]. Similarly, G for pyroxene and ilmenite[35] are 2.91×10^{-8} mm s^{-1} and 1.34×10^{-8} mm s^{-1}, respectively. These growth rates were also previously used in the study of CSD of Apollo samples[57]. For the convenience of comparison with different minerals and Apollo samples, we did not use different growth rates for different sizes of crystals. These values could be appropriate for the microlites (Population 1 and Population 2). However, we must bear in mind that some large crystals with slower cooling should have a lower G (ref. [33]); thus, the residence time calculated by a unified G (~10^{-8} mm s^{-1}) is a lower limit.

Clinopyroxene thermobarometer

Clinopyroxene–liquid thermobarometers[26,29] were applied to constrain the magma storage P–T conditions. All calculations were carried out through the Microsoft Excel spreadsheet of Clinopyroxene_P-T_2020 v.3 available online[26,29]. Clinopyroxene from the CE-5 samples display a larger variation (Mg# = 1–62) (Extended Data Fig. 3a), which is caused by composition change or analytical error. To get robust P–T results for magma origin and storage, some rigorous strategies have been used to evaluate data quality and to test clinopyroxene–liquid equilibrium[26,29]. First, the total cations of clinopyroxene compositions were calculated on the basis of six oxygens. As suggested by Neave and Putirka[26], analytical errors can affect the results of the thermobarometers. Thus, analysed spots with cation sums of <3.98 or >4.02 and very low Na contents (Jd < 0.002), below the detection limit, were excluded. Second, Neave and Putirka[26] also suggested that some low Al (total < 0.11) clinopyroxenes could experience Ca and Al dilution caused by the disequilibrium incorporation of Mg and Fe during their rapid growth, and thus these grains were removed. Mollo et al.[58] also suggested that crystallization of basaltic magmas at a high degree of undercooling would lead to the enrichment of Al, Na and Ti in clinopyroxene. Clinopyroxenes with some disequilibrium textures (for example, skeletal, dendritic, microcrystalline and quenched rims) indicating rapid dynamic crystallization on the lunar surface were also excluded.

In this study, only clinopyroxene grains with high Mg# values (50–62) that crystallized at a relatively early stage were chosen to calculate the magma storage P–T conditions (Extended Data Fig. 3a,b). Using Kd_{Fe-Mg} values for clinopyroxene (0.27 ± 0.03) (ref. [29]), the high-Mg# (50–62) clinopyroxenes from the CE-5 samples could be crystallized from basaltic magmas with Mg# = 21–32 (average = 26) (Extended Data Fig. 3c). The chemical composition of sample CE-5 B1 with Mg# of 26 (ref. [12]) (Extended Data Table 3) could represent a suitable equilibrium liquid. In the Rhodes Diagram (Extended Data Fig. 3c), all the analysis points used to calculate the P–T conditions fall within the error line of the equilibrium with the host melt. Further, all the predicted calcium Tschermak, enstatite–ferrosilite and diopside–hedenbergite components should fall near the 1:1 line with observed components[29]

(Extended Data Fig. 3d). The predicted clinopyroxene components are calculated using the Putirka equations[59], which were constructed by fitting experimental pyroxene-melt pairs by the least squares method. After all the preceding conditions were met, the results of the equation for pressure from ref. [26] and the equation for temperature from ref. [29] were applied. The standard errors of estimates for temperature and pressure are ±33 °C and ±1.4 kbar (refs. [26,29]), respectively. In addition, as the magma composition of lunar basalts differs from that of terrestrial basalts, clinopyroxene thermobarometers based on experimental petrological data of terrestrial basalts may have extra uncertainty.

Diffusion modelling

Clinopyroxenes display diverse zoning types, including patchy (II), normal (III-a) and reverse (III-b) zoning (Fig. 2 and Extended Data Fig. 2). Experiments have demonstrated that the outside thin rims of minerals were modulated by the growth, rather than diffusion[37]. Thus, the outermost thin rims of clinopyroxenes cannot be used to calculate the diffusion time. Mg# (100 × molar Mg/(Mg + Fe)) diffusion profiles for Type II and Type III clinopyroxene were used to estimated pre-eruption residence times[36]. Previous studies have used the greyscale of BSE images of clinopyroxene as a proxy for Mg# (ref. [60]). However, Ca contents in clinopyroxene can also affect the greyscale of BSE images[61]; thus, the relationship between greyscale and Mg# or Ca contents is given in Extended Data Fig. 4. The results indicate that Mg# in clinopyroxene has a better linear correlation with the greyscale than those of Ca contents, implying the effect of Ca is insignificant. Thus, the high spatial resolution of BSE images could be a very effective method of extracting the timescale information at the nanoscale[60,62]. The image-processing software of ImageJ was used to transform greyscale and pixel into composition and distance. The BSE grey values, the distance from the rims and the corresponding Mg# values for some representative profiles for different types of clinopyroxenes are given in Supplementary Table 3.

A common solution using error function for the one-dimension diffusion problem[25,63] was used to simulate the diffusion behaviour of Mg# in Cpx and to calculate the residence time:

$$C = \frac{C_1 + C_2}{2} + \frac{C_2 - C_1}{2} \times \mathrm{erf}\left(\frac{x}{2\sqrt{Dt}}\right) \quad (2)$$

where C is concentration, x is the half diffusion width and D is the diffusion coefficient; C_1 and C_2 represent the initial concentration of the two endmembers before diffusion; and erf means error function. The diffusion time (t) can be estimated by fitting a model to the concentration profile as suggested by several authors[25,63]. We have used MATLAB software to solve the preceding diffusion equations. To get a best-fit time, the mean-square-root method[25] was used to fit the optimal curve. The error calculation uses the same method as suggested by ref. [64].

D_{Fe-Mg} in clinopyroxene is strongly dependent on the temperature[36] (Extended Data Fig. 5a). Since most clinopyroxene with complex zoning formed in the deep magma reservoirs, we assume that it is most likely at a peak pressure of 4 kbar. pMELTs simulation results at 4 kbar suggest that the Mg# values of clinopyroxene show a good correlation with temperature (Extended Data Fig. 5b). Therefore, we utilized the Mg# of clinopyroxene to constrain the crystallization temperature.

For pyroxene, D_{Fe-Mg} along the [001] axis is typically 3.5 times faster than along the [100] and [010] axes[61]. Due to diffusion anisotropy in clinopyroxene, it is necessary to determine the crystallographic orientation of the profile to calculate $D_{profile}$(ref. [65]).

$$D_{profile} = D_{[100]} \times (\cos\alpha)^2 + D_{[010]} \times (\cos\beta)^2 + D_{[001]} \times (\cos\gamma)^2 \quad (3)$$

where α, β and γ are the angles between the measured profile and the [100], [010] and [001] axes, respectively. The crystallographic orientation of clinopyroxene and the angles between the profile and the three axes were measured by electron backscatter diffraction (EBSD, see the following section). Some representative EBSD results are given in Fig. 2, Extended Data Fig. 2 and Extended Data Table 2.

Electron backscatter diffraction (EBSD)

Clinopyroxene crystallographic axes were measured on a Zeiss Sigma 300VP scanning electron microscope and an Oxford Instruments Aztec Symmetry EBSD detector at the School of Earth Sciences, China University of Geosciences, Wuhan. Working conditions were as follows: 15 kV accelerating voltage, ~0.5–1.0 μm spot size, working distance of 16 mm, 70° sample tilt angle and low-vacuum mode of 15 Pa. Diffraction patterns were collected and indexed with an automatic mapping mode using the Aztec 6.0 software from Oxford Instruments. To assure data quality, only those measurements with mean angular deviation values below 1° were accepted for analyses.

pMELTS simulations

To investigate the crystallization history and the nature of the source region of the CE-5 basalts, pMELTS equilibrium crystallization simulations were carried out over a range of pressures (0–15 kbar) and temperatures (900–1,400 °C) at f_{O2} = ΔIW buffer[28]. According to the mineral assemblage of the CE-5 basalts[13,19,20], the crystalline phases are mainly clinopyroxene, plagioclase, olivine and ilmenite. Some minor mineral phases (for example, spinel and apatite) are excluded in the simulations. The mineralogical and geochemical data suggested that the CE-5 basalts are highly evolved magmas with extensive fractional crystallization (~45–70%)[13]. Thus, the average composition of CE-5 basaltic fragments (CE-5A) cannot represent the primitive magma. A CE-5 basaltic fragment (042GP-002) with high Mg# (47) values could represent a primitive sample. Recently, the Sr–Nd isotopic composition[13] and the Ti concentration in olivine[22] of the CE-5 basalts also suggested that the magma source of the CE-5 basalts is very similar to the Apollo 12 low-Ti basalts. Therefore, the average composition of CE-5 basaltic fragments[18,20] (CE-5A), the relative primitive basaltic fragment (042GP-002) and the Apollo 12 nearly primary low-Ti basaltic sample 12002 (Extended Data Table 3) were used as starting materials, respectively. The Apollo 12 sample 12002 had been well studied by experimental petrology[40,42]; this provided a good basis to compare the results of pMELTS simulation and to evaluate the effectiveness of the simulation results. The pMELTS results for 12002 concerning the phase diagram and melt composition are consistent with those of the experimental results[40] (Extended Data Fig. 6a,b and Fig. 4b).

Data availability

All data analysed or generated during this study are available in EarthChem Library at https://doi.org/10.26022/IEDA/112769, Science Data Bank at https://doi.org/10.57760/sciencedb.o00009.00468 and Supplementary Tables. Source data are provided with this paper.

Code availability

The MATLAB code used for diffusion modelling and error calculation in this study can be obtained from the corresponding author B.L.

References

53. Cashman, K. V. & Marsh, B. D. Crystal size distribution (CSD) in rocks and the kinetics and dynamics of crystallization II: Makaopuhi lava lake. *Contrib. Mineral. Petrol.* **99**, 292–305 (1988).
54. China National Space Administration. *Lunar Sample Information Database* (2023); https://moon.bao.ac.cn/moonSampleMode/index.html
55. Morgan, D. J. & Jerram, D. A. On estimating crystal shape for crystal size distribution analysis. *J. Volcanol. Geotherm. Res.* **154**, 1–7 (2006).
56. Higgins, M. D. Measurement of crystal size distributions. *Am. Mineral.* **85**, 1105–1116 (2000).

57. Donohue, P. H. & Neal, C. R. Quantitative textural analysis of ilmenite in Apollo 17 high-titanium mare basalts. *Geochim. Cosmochim. Acta* **149**, 115–130 (2015).
58. Mollo, S., Del Gaudio, P., Ventura, G., Iezzi, G. & Scarlato, P. Dependence of clinopyroxene composition on cooling rate in basaltic magmas: implications for thermobarometry. *Lithos* **118**, 302–312 (2010).
59. Putirka, K. Clinopyroxene+liquid equilibria to 100 kbar and 2450 K. *Contrib. Mineral. Petrol.* **135**, 151–163 (1999).
60. Morgan, D. J. et al. Time scales of crystal residence and magma chamber volume from modelling of diffusion profiles in phenocrysts: Vesuvius 1944. *Earth Planet. Sci. Lett.* **222**, 933–946 (2004).
61. Dohmen, R., Faak, K. & Blundy, J. D. Chronometry and speedometry of magmatic processes using chemical diffusion in olivine, plagioclase and pyroxenes. *Rev. Mineral. Geochem.* **83**, 535–575 (2017).
62. Saunders, K., Buse, B., Kilburn, M. R., Kearns, S. & Blundy, J. Nanoscale characterisation of crystal zoning. *Chem. Geol.* **364**, 20–32 (2014).
63. Zhang, Y. *Geochemical Kinetics* (Princeton University Press, 2009).
64. Costa, F. Clocks in magmatic rocks. *Annu. Rev. Earth Planet. Sci.* **49**, 231–252 (2021).
65. Costa, F. & Morgan, D. in *Timescales of Magmatic Processes: From Core to Atmosphere* (eds Dosseto, A., Turner, P.A. & Van Orman, J.A.), Ch. 7 (John Wiley & Sons, 2010); https://doi.org/10.1002/9781444328509.ch7

Acknowledgements

We appreciate all staff of the Chang'e-5 mission, and their great effort makes this work possible. We thank China National Space Administration (CNSA) for providing access to the returned sample (CE5C0400) and China University of Geoscience, Wuhan for technical support. This work was supported by the pre-research project on Civil Aerospace Technologies funded by CNSA to Z. W. (no. D020205). B.L. thanks the China Scholarship Council (no. 201906415001) and K. Cashman, J. Blundy and A. Rust for guiding volcanology research.

Author contributions

Z.W. applied the CE-5 samples from CNSA with the help of Q.H., X.W., K.Z., Z.H., L.X., W.Z. and Z.S., and B.L. and Z.W. designed this research. Q.H., Y.L., X.W. and J.Z. prepared the samples. B.L., B.R., J.S., B.H., Y.H., C.X., F.P. and W.L. carried out experiments. B.L. and Z.W. wrote the manuscript draft, Y.Q., J.W.H., F.M., L.X., H.B., H.Z. and L.X. revised the manuscript, and all authors participated in data interpretation.

Competing interests

The authors declare no competing interests.

Additional information

Extended data is available for this paper at https://doi.org/10.1038/s41561-023-01146-x.

Supplementary information The online version contains supplementary material available at https://doi.org/10.1038/s41561-023-01146-x.

Correspondence and requests for materials should be addressed to Biji Luo or Zaicong Wang.

Peer review information *Nature Geoscience* thanks Charles Shearer, Renaud Merle and the other, anonymous, reviewer(s) for their contribution to the peer review of this work. Primary Handling Editor: Tamara Goldin, in collaboration with the *Nature Geoscience* team.

https://doi.org/10.1038/s41561-023-01146-x

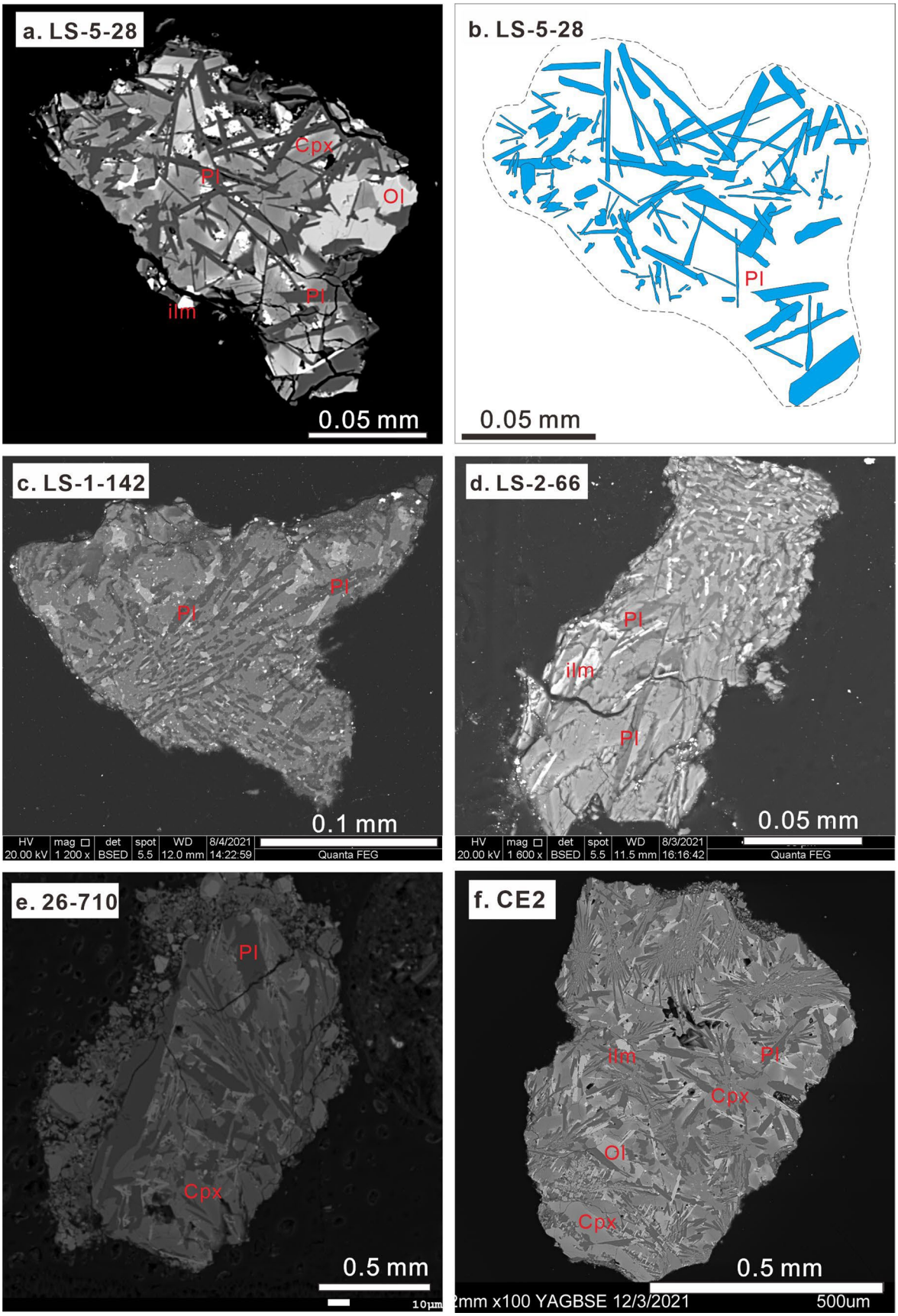

Extended Data Fig. 1 | Some reprehensive backscattered electron (BSE) images of the Chang'E-5 basalt clasts in this study were used for CSD analyzed. **a**–**e**, Microlites in groundmass. a. LS-5-28. b. Outline of plagioclase in LS-5-28. c. LS-1-142. d. LS-2-66. e. 26-710. f. Porphyritic, CE-2. Cpx, clinopyroxene; Pl, plagioclase; Ol, olivine; Ilm, ilmenite.

https://doi.org/10.1038/s41561-023-01146-x

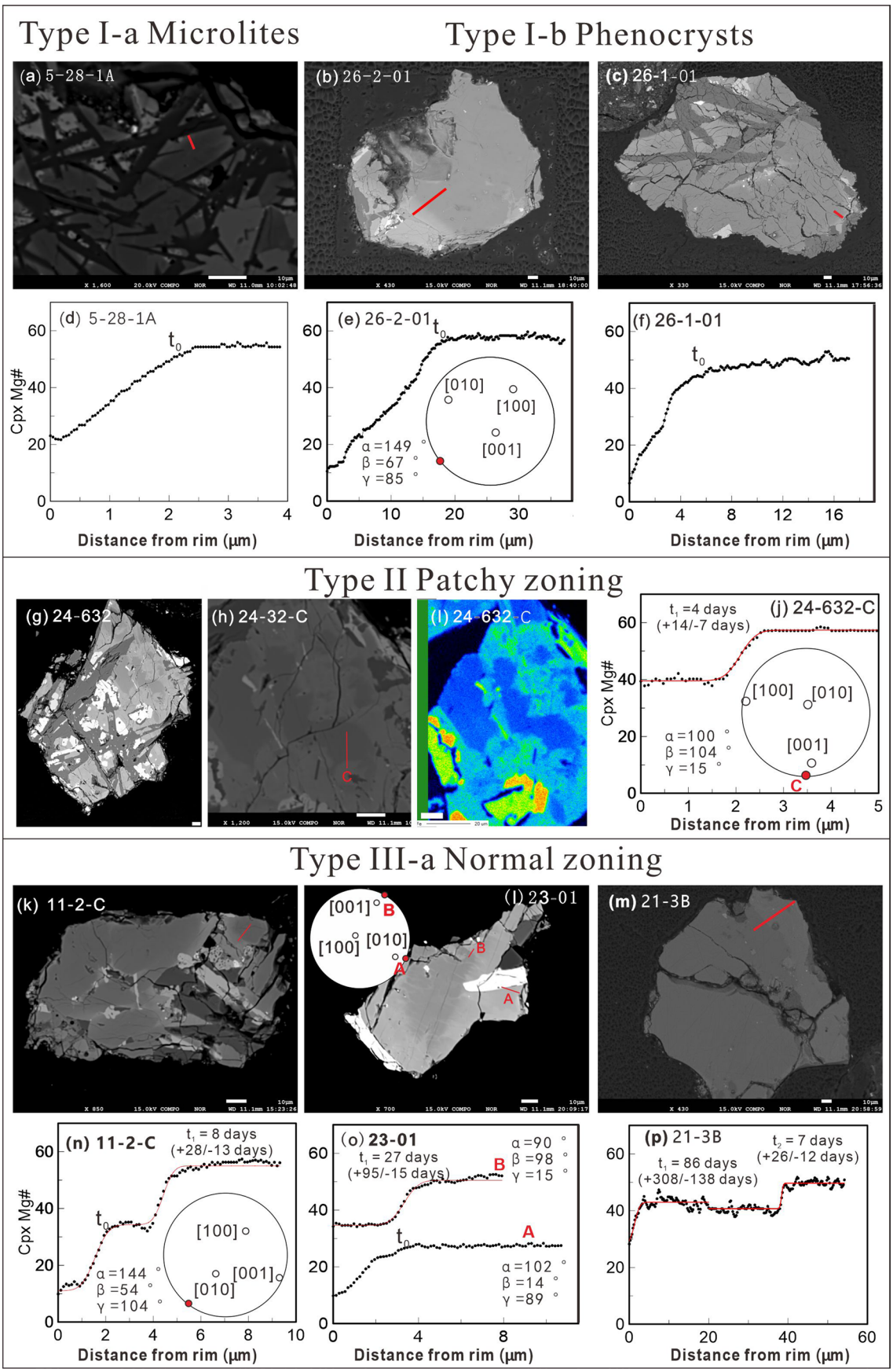

Extended Data Fig. 2 | Representative textural and compositional zoning diagrams for different types of clinopyroxene. Type I-a, microlites: a, d, 5-28-1A; Type I-b, larger phenocrysts: b, e, 26-2-01; and c f, 26-1-01; Type II, patchy zoning, g-j, 24-632-C; Type III-a, normal zoning: k, n, 11-2-C; l, o, 23-01; and m, p, 21-3B. Insert circles represent the crystallographic and traverse orientation projection that were measured by EBSD. α, β and γ are angles between measured profile and [100], [010] and [001] axes, respectively. The white bars represent 10 μm.

https://doi.org/10.1038/s41561-023-01146-x

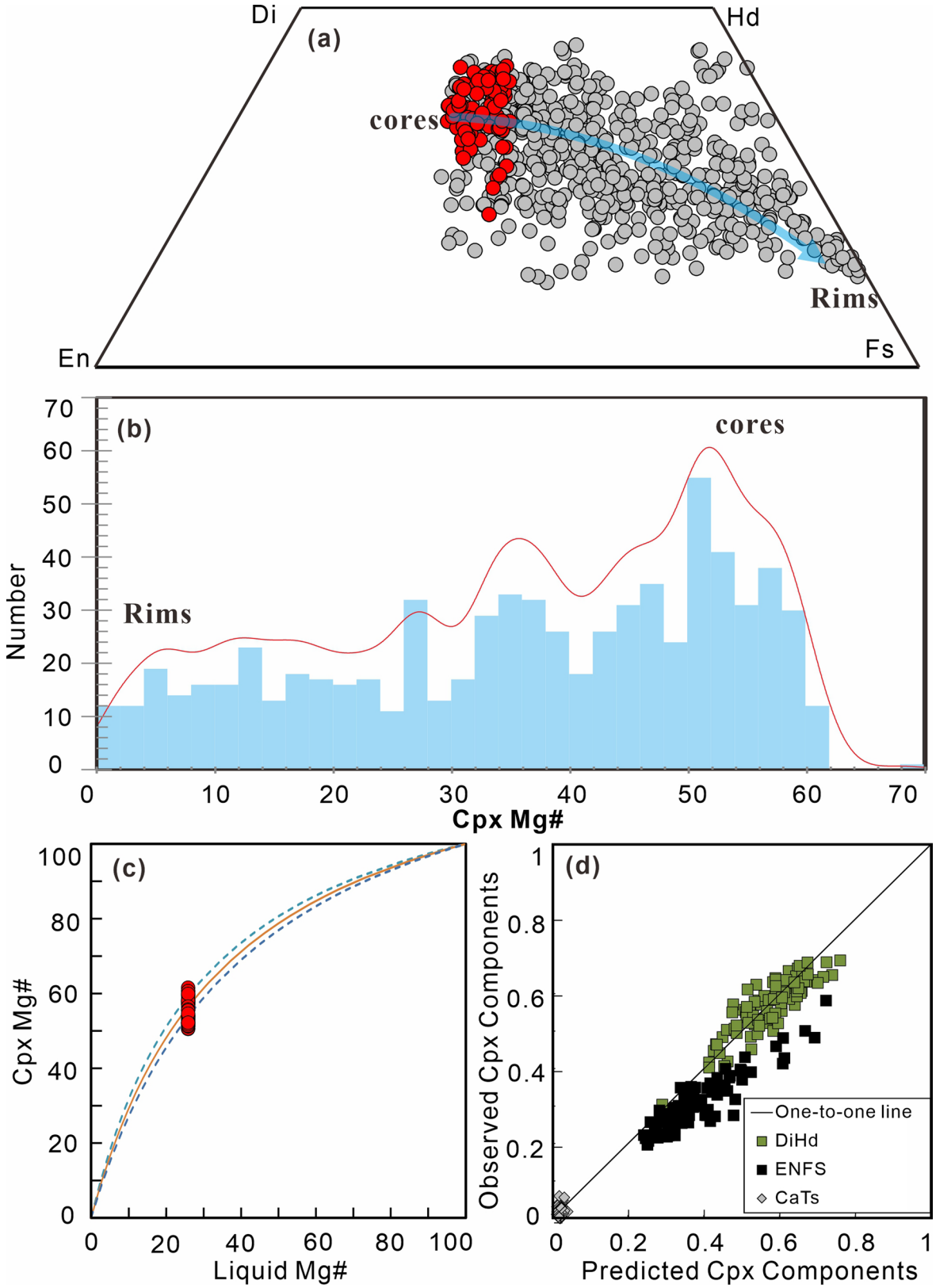

Extended Data Fig. 3 | Chemical composition of clinopyroxene from the Chang'E-5 basaltic fragments. a, Quadrilateral diagram of clinopyroxene (Cpx). The grey dots are all the original CPX analysis points (data are from this study and references[12–14,19]). The red dots are the relatively high Mg# analysis points and were used for the calculations of clinopyroxene-liquid thermobarometers. **b**, Histogram showing the distribution of the Mg# values of clinopyroxene. **c**, Rhodes diagram for the clinopyroxene. Cpx Mg# vs. Liquid Mg#. The composition of CE-5 B1[12] that equilibrium with most high Mg#-Cpx was used to represent the composition of the liquid. **d**, Observed Cpx components vs. Predicted Cpx components. The observed Cpx components are close to the predicted Cpx components, indicating that the calculation results are reliable. CaTs: calcium Tschermak, En: enstatite, Fs: ferrosilite, Di: diopside, Hd: hedenbergite.

https://doi.org/10.1038/s41561-023-01146-x

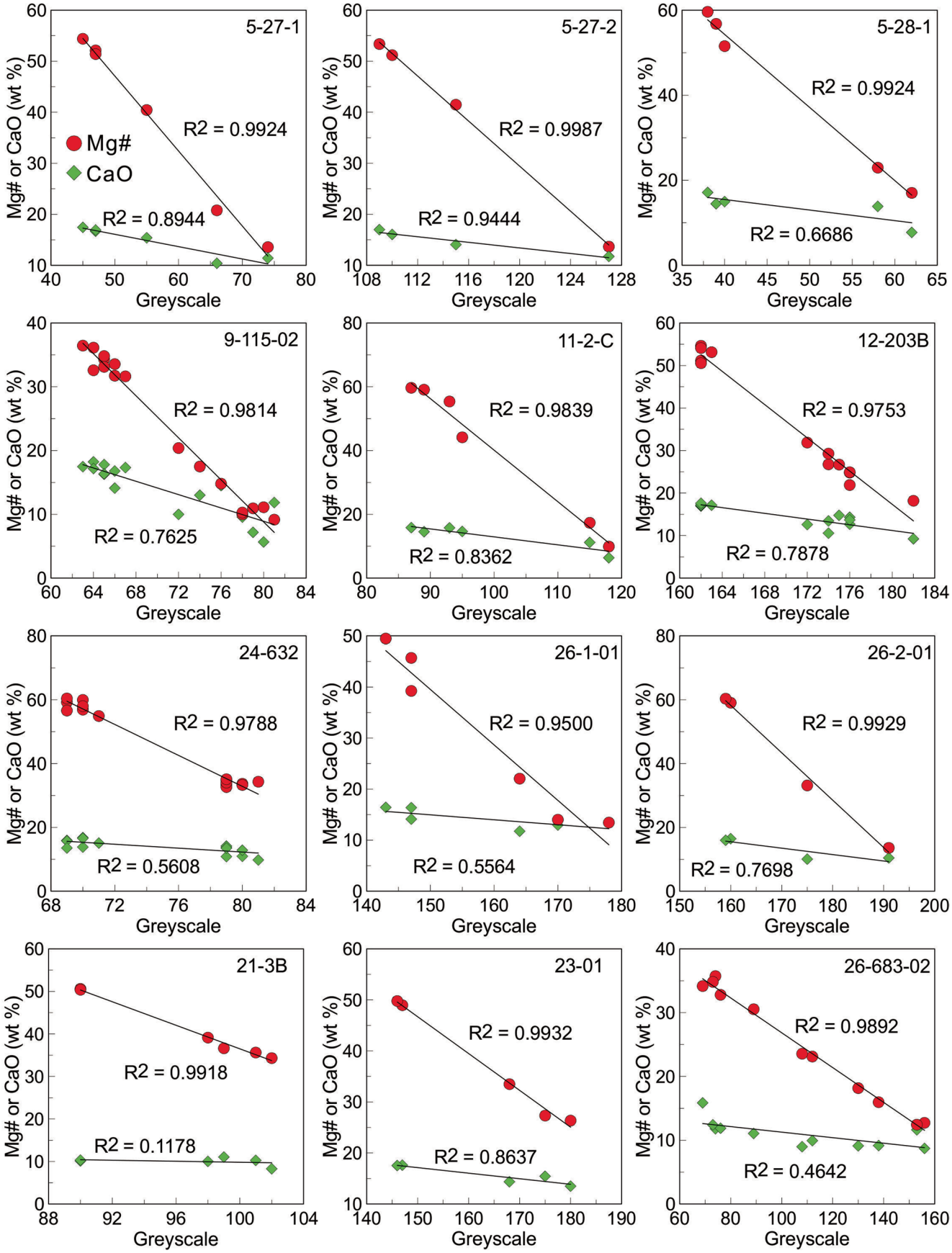

Extended Data Fig. 4 | The relationship between greyscale and Mg# and CaO (wt. %) for clinopyroxene. The results show that the greyscale is mainly controlled by Mg# values, rather than CaO contents.

https://doi.org/10.1038/s41561-023-01146-x

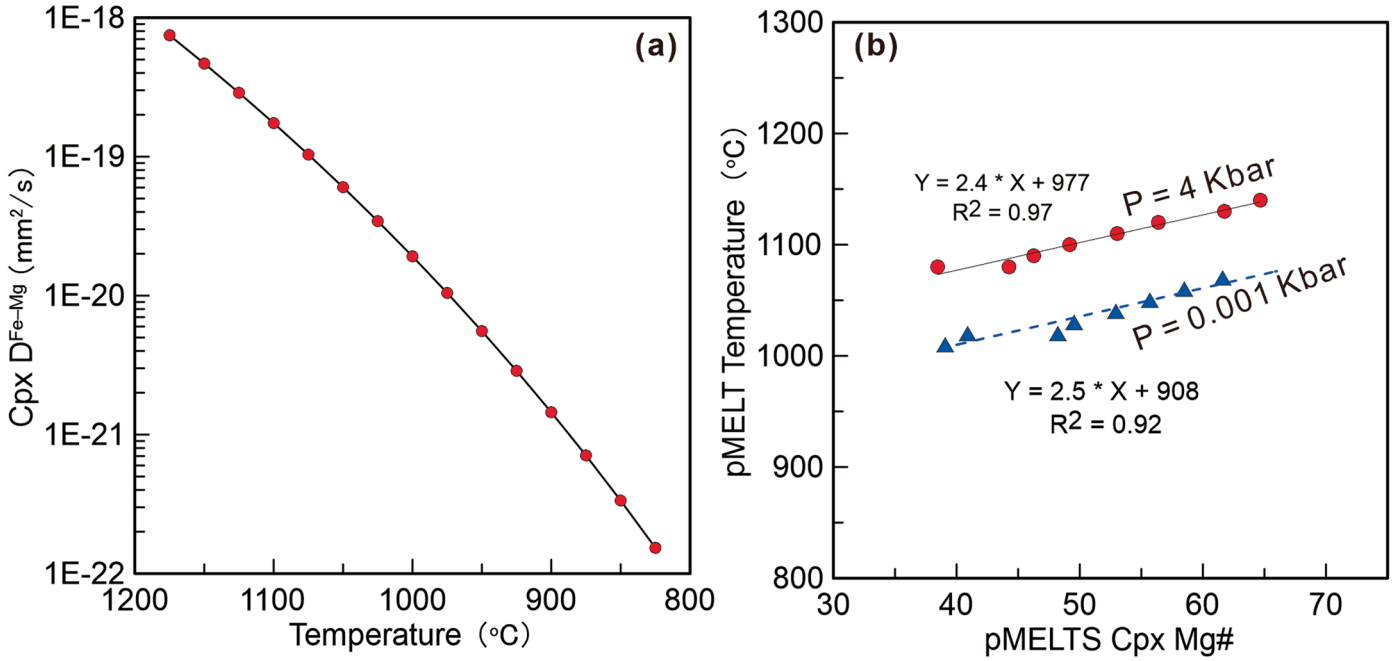

Extended Data Fig. 5 | Diffusion coefficient and temperature calculations. **a**, Diffusion coefficients D_{Fe-Mg} of clinopyroxene verses temperature (°C)[36]. **b**, pMELTs simulation results of Mg# values of clinopyroxene and temperatures at P = 0.001 kbar and P = 4 kbar, respectively. The average compositions of the CE-5 basaltic fragments (CE-5A)[13] were used as starting material. The result show that the Mg# values of clinopyroxene have a good relationship with the temperature. Thus, the Mg# values of clinopyroxene can be used to estimate the crystallization temperature. Since most clinopyroxene with complex zoning formed in the deep magma reservoirs, we assume that it is most likely at a peak pressure of 4 kbar.

https://doi.org/10.1038/s41561-023-01146-x

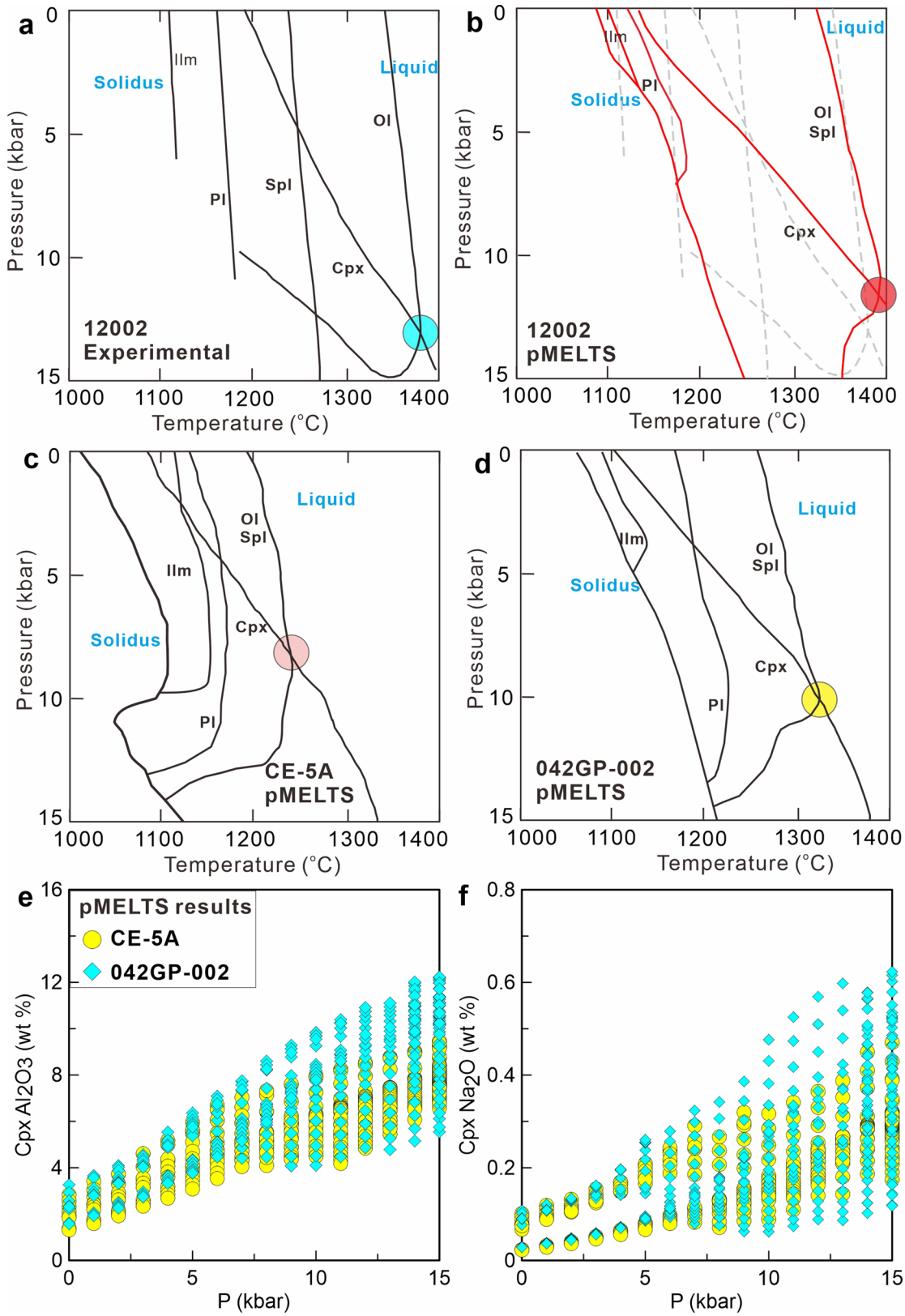

Extended Data Fig. 6 | pMELTs simulation results. a, Experimental phase diagram for the Apollo-12 nearly primary low-Ti basaltic sample 12002[40]. **b**–**d**, The phase diagrams were simulated by pMELTs for the 12002, CE-5A, and 042GP-002, respectively. The shaded circles in a, b, c and d represent the multiple-saturation points, which could indicate the potential minimum origin depth and residual minerals[43]. The grey lines in b are the experimental result for 12002[40]. The pMELTS simulation phase diagram for 12002 is very similar to that of the experimental result[40], indicating that the pMELTS results are effective. The results suggest that the CE-5 basalts were saturated with olivine and pyroxene residual at deep source. e and f, pMELTS results for clinopyroxene Al_2O_3 or Na_2O contents vs. pressures, respectively. CE-5A is the average composition of CE-5 basaltic fragments[13]. 042GP-002 is a relatively primitive basaltic fragment with higher Mg# (47) value[13]. Cpx, clinopyroxene; Pl, plagioclase; Ol, olivine; Ilm, ilmenite; Spl, spinel.

https://doi.org/10.1038/s41561-023-01146-x

Extended Data Table 1 | Summary of CSD slopes, intercepts, characteristic length (C_L) and calculated residence time (τ) of plagioclase, ilmenite and clinopyroxene from the Chang'E-5 basaltic fragments

Sample	Population and texture	Crystal total	Area (mm^2)	Intercept $ln(mm^{-4})$	CSD Slope	R^2	C_L* (mm)	τ& (days)	2*SD +/-
Plagioclase									
LS-5-28^T	1, Microlite	183	0.004	18.95	-133.8	0.975	7.5E-03	3	1/1
LS-2-66^T	1, Microlite	241	0.003	18.75	-106.5	0.956	9.4E-03	4	2/1
LS-1-142^T	1, Microlite	375	0.007	18.68	-105.6	0.987	9.5E-03	4	1/1
26-710^T	1, Microlite	161	0.004	17.00	-56.3	0.986	1.8E-02	8	7/3
103-001, 003[11]	2, Porphyritic	246	0.461	9.95	-12.0	0.974	8.3E-02	39	11/7
103-001, 007[13]	2, Porphyritic	226	0.113	12.36	-24.4	0.994	4.1E-02	19	2/2
070GP01^N	2, Porphyritic	258	1.144	8.46	-9.7	0.998	1.0E-01	48	3/3
103-003, 013[13]	2, Porphyritic	168	0.103	10.49	-11.8	0.956	8.5E-02	39	17/9
007GP01^N	2, Subophitic	378	0.279	10.44	-12.8	0.988	7.8E-02	36	9/6
CE-2^T	2, Porphyritic	639	0.143	13.45	-27.8	0.917	3.6E-02	17	9/4
007GP02^N	3, Porphyritic	271	1.177	7.10	-5.8	0.966	1.7E-01	81	22/14
041GP, 001[13]	3, Subophitic	151	1.245	6.93	-5.2	0.995	1.9E-01	90	8/7
042GP, 001[13]	3, Subophitic	203	1.708	6.76	-5.1	0.974	2.0E-01	91	27/17
007GP02^N	3, Subophitic	362	1.454	6.58	-4.4	0.981	2.3E-01	105	25/17
CE5-B1[12]	3, Finegrained	277	1.933	7.25	-6.5	0.974	1.5E-01	71	21/13
Clinopyroxene									
042GP, 001[13]	2, Subophitic	266	1.584	10.39	-20.0	0.967	5.0E-02	20	10/5
103-001,003[11]	2, Porphyritic	281	0.407	12.55	-39.6	0.989	2.5E-02	10	2/2
070GP01^N	2, Porphyritic	161	1.274	9.16	-16.0	0.953	6.3E-02	25	52/10
007GP02^N	2, Subophitic	626	0.394	10.91	-29.2	0.913	3.4E-02	14	18/5
CE5-B1[12]	2, Finegrained	218	1.724	9.89	-22.7	0.992	4.4E-02	17	6/4
Ilmenite									
103-001, 003[11]	2, Porphyritic	228	0.190	10.83	-20.1	0.975	5.0E-02	41	17/9
103-001, 007[13]	2, Porphyritic	282	0.038	13.61	-49.0	0.982	2.0E-02	17	4/3
070GP02^N	2, Porphyritic	303	0.558	8.90	-16.6	0.985	6.0E-02	50	10/7
042GP, 001[13]	3, Subophitic	262	0.629	7.89	-8.7	0.944	1.2E-01	96	49/24
007GP01-02^N	3, Subophitic	279	0.698	8.07	-10.5	0.948	9.5E-02	79	29/17

Some reprehensive BSE images of samples in this study are given in the Extended Data Fig. 1. The crystal length (long axis) of population 1 mineral is less than 0.1 mm. The population 2 minerals have crystal length between 0.1 and 0.5 mm. The population 3 minerals have maximum crystal length above 0.5 mm. *C_L = −1/slope; &τ = −1/G*Slope. G is the growth rate of minerals. T, this study; N, these BSE images were obtained from the China National Space Administration (https://moon.bao.ac.cn/moonSampleMode/index.html); and others are from references[11–13]. Experimentally determined growth rates for plagioclase ($2.49*10^{-8}$ mm/s), clinopyroxene ($2.91*10^{-8}$ mm/s) and ilmenite ($1.35*10^{-8}$ mm/s) in basalts[35] were used in this study.

https://doi.org/10.1038/s41561-023-01146-x

Extended Data Table 2 | Calculated residence times (days) obtained by modeling Fe-Mg diffusion in clinopyroxene from the Chang'E-5 basaltic fragments

Sample	Type	α	β	γ	$Mg\#_1$	$Mg\#_2$	T (°C)	D_{Fe-Mg}	D*profile*	t (Days)	1*SD (+/-)	R^2
9-115-2C	I-a	104	64	153	11	35						
5-27-1A	I-b	22	115	102	10	50						
11-1-A	I-b	145	58	61	15	56						
11-1-B	I-b	116	33	103	15	56						
26-2-01	I-b	149	67	85	10	60						
24-632-A	II	54	102	54	32	55	1056	6.6E-20	5.8E-20	74	259/118	0.980
24-632-C	II	100	104	15	40	55	1073	9.9E-20	1.0E-19	4	14/7	0.993
5-27-2	III-a	164	87	90	28	42	1044	5.3E-20	2.5E-20	198	693/317	0.928
	III-a	164	87	90	42	54	1078	1.1E-19	5.3E-20	13	44/20	0.957
11-2-C	III-a	144	54	104	33	57	1056	6.9E-20	8.7E-20	8	28/13	0.969
23-1-B	III-a	90	98	15	35	50	1061	7.7E-20	6.3E-20	27	95/43	0.987
23-1-A	III-a	102	14	89	10	27						
21-3-B	III-a				34	42	1057	7.3E-20		86	301/138	0.804
	III-a				42	50	1078	1.1E-19		7	26/12	0.942
12-203B	III-b	121	30	84	55	33	1109	2.1E-19	9.8E-20	10	35/16	0.992
	III-b	121	30	84	30	55	1049	5.9E-20	2.8E-20	1461	5114/2338	0.973

The BSE images and profiles of reprehensive samples are given in the Fig. 2 and Extended Data Fig. 2. Type I-a, microlites; I-b, large phenocrysts; Type II, patchy zoning; Type III-a, normal zoning and Type III-b, reverse zoning. α, β, and γ are angles between the measured profile and [100], [010] and [001] axes, respectively. D_{Fe-Mg} and $D_{profile}$ is diffusion coefficient along the [001] axis and the profile, respectively. The error calculation uses the same method as suggested by[64].

https://doi.org/10.1038/s41561-023-01146-x

Extended Data Table 3 | Major elements of some representative Chang'E-5 basaltic fragments and lunar soils and Apollo 12 basalt 12002

Major elements	CE-5 Basaltic fragments		CE-5 average basalts fragments	average CE-5 lunar soil		Apollo 12 basalt
	CE5-B1[12]	042GP-002[13]	CE-5A[13]	CE-5S[20]	CE-5S[18]	12002[42]
SiO_2	42.58	42.4	42.1	42.2	41.25	43.56
TiO_2	6.26	3.1	5.7	5.0	5.12	2.6
Al_2O_3	10.59	12.0	11.6	10.8	11.55	7.87
Cr_2O_3	0.14	0.3	0.2	0.18	0.21	0.96
FeO	23.05	19.8	22.2	22.5	22.7	21.66
MnO	0.3	0.0.2	0.3	0.28	0.28	0.288
MgO	4.58	9.7	5.8	6.48	6.52	14.88
CaO	11.87	10.7	10.9	11.0	11.64	8.26
Na_2O	0.35	0.5	0.6	0.26	0.46	0.23
K_2O	0.07	0.04	0.1	0.19	0.21	0.051
P_2O_5	0.21	0.2	0.2	0.23	0.27	0.11
Total	100	99.1	99.7	98.94	100.21	100.47
Mg#	26	47	32	34	34	55

Note: the numbers on fragments represent references.